JOURNAL OF COMPUTATIONAL PHYSICS 105, 133–149 (1993)

Transition to Chaos in an Open Unforced 2D Flow

THOMAS H. PULLIAM AND JOHN A. VASTANO

NASA Ames Research Center, Moffett Field, California 94035

Received January 18, 1991; revised July 13, 1992

Unsteady low Reynolds number flow past a two-dimensional airfoil is studied numerically. The purpose is to (1) determine the bifurcation sequence leading from simple periodic flow to complex aperiodic flow as Reynolds number is increased, (2) identify and quantify the chaos present in the aperiodic flow, and (3) evaluate the role of numerics in modifying and controlling the observed bifurcation scenario. The full two-dimensional Navier–Stokes equations are solved for a NACA 0012 airfoil at $M_\infty = 0.2$, $\alpha = 20°$, and $\mathrm{Re} < 4000$. The Navier–Stokes code ARC2D in an unsteady time-accurate mode is used for most of the computations. For each Reynolds number studied, the asymptotic behavior of the flow is studied using time delay reconstructions, Poincaré sections, and frequency decompositions. The system undergoes a period-doubling bifurcation to chaos as the Reynolds number is increased from 800 to 1600, with windows of periodic behavior in the chaotic regime past 1600. The observed chaotic attractors are further characterized by estimates of the fractal dimension and partial Lyapunov exponent spectra. Tests are made on the effects of varying mesh resolution, added artificial dissipation, and order of spatial or temporal accuracy of the numerical method. It is shown that the observed chaos does not arise due to numerical effects alone, but is a true solution of the model system. Local Lyapunov exponent analysis is used to determine the physical mechanism behind the period-doublings.

I. INTRODUCTION

It is a mathematical fact that aperiodicity can in some cases be described as motion on a low-dimensional chaotic phase space attractor. The concept of chaos was originally brought into the physical sciences as a means of describing turbulent fluid flows [1]. Low-dimensional chaos has now been observed in a wide range of hydrodynamic systems. These include simple models of flows (e.g., the Lorenz equations [2, 3]), experimental flows (e.g., Taylor–Couette flow [4]), and more recently in numerical simulations (e.g., Taylor–Couette flow [5] and turbulent plane channel flow [6]). Most of the cases studied to date are closed flow systems or open flow problems with forcing [7]. There have been no reports of unforced open flow experiments showing low-dimensional chaotic behavior. Chaotic solutions *have* been observed in several two-dimensional numerical simulations of open flow systems at low Reynolds numbers and low Mach numbers. For example, Fortin *et al.* [8] presented results for a cascade flow simulation which exhibited a region of chaos as a function of Reynolds number. Ghia *et al.* [9] have examined high angle of attack incompressible airfoil simulations with chaotic solutions at low Reynolds numbers. What is lacking is a complete bifurcation scenario demonstrating the transition to low-dimensional chaos for a numerically computed open flow. Once such a system is in hand, then the variety of difficult questions concerning the definition of attractors for open flow systems can be addressed in a systematic fashion.

The open flow system studied here is compressible flow over a two-dimensional airfoil at high angle of attack and low Mach number. The particular case is a NACA 0012 airfoil at angle of attack $\alpha = 20°$ and Mach number $M_\infty = 0.2$. The bifurcation parameter is the Reynolds number, which is varied in the range $600 \leqslant \mathrm{Re} \leqslant 3500$. In this range the flow is unsteady and flowfield visualizations show a shear layer off the leading edge, massive separation over the upper surface, and trailing edge vortices. These common features simplify the comparison of flows at different Reynolds numbers: no fundamentally new flow features appear, so the principle differences between flows are in temporal evolution, not spatial evolution.

The numerical model used in this study is discussed in Section II with a brief description of the various parameters of the algorithm that affect the results. The bifurcation diagram obtained for a "standard" algorithm is presented in Section III. The effects of mesh refinement and algorithm parameter variation on the observed bifurcation sequence, comparisons using other numerical codes, and the possibility that the observed chaos is numerically generated are discussed in Section IV. The chaotic states observed past the transition are analyzed in Section V, and Section VI contains a summary of the results as well as some concluding remarks. A demonstration of numerically generated chaos for a simple model equation is included in an appendix.

0021-9991/93 $5.00

II. NUMERICAL MODEL

The model equations are the full two-dimensional Navier–Stokes equations. The numerical code used here, ARC2D [10], solves these equations in strong conservation law form and general curvilinear coordinates. A first- or second-order-accurate in time approximate factorization scheme with second- or fourth-order-accurate space differences is employed. For smooth geometries with adequate mesh resolution there would be no need for artificial dissipation at the low Reynolds numbers used here. Nondissipative central differences, along with the viscous terms, are adequate in such cases to stably compute the flows. However, the sharp trailing edge of the airfoil, coupled with the highly energetic nature of the flows computed, necessitates the use of some form of artificial dissipation. For most of the results presented, a low amount of artificial dissipation is added to stabilize the computations [11]. Zero velocity, adiabatic wall conditions are used at the airfoil surface and characteristic boundary conditions are used at the free boundaries.

Three successively finer "C" type topology meshes (grids) are employed with designations **A** (169 × 49), **B** (369 × 89), and finally **C** (849 × 161). Grid **A** is shown in Fig. 1. Mesh points were distributed equally between the airfoil surface and the wake, since both the local flow structure near the airfoil and the shed vortices downstream of the airfoil are of interest. For example, grid **C** has 200 points in the wake in the streamwise direction. The outer boundary locations were placed at 12 chords from the airfoil and the normal spacing at the surface was varied from 0.01 for grid **A**, 0.005 for **B**, and 0.002 for **C**. At the Reynolds numbers of interest these mesh distributions give a reasonable mesh refinement sequence.

The time step used was $\Delta t = 0.05$, which corresponds to free stream flow traveling one chord in 100 iterations, $N = 100$. Sensitivity to initial conditions was studied by starting from various initial solutions; for example, some cases were impulsively started from free stream and then compared with cases started from fully developed flow at a lower or higher Reynolds number. In all cases examined here the results were independent of the initial conditions. The runs were performed on CRAY2 and CRAY-YMP computers and typically required 4 to 8 h of CPU time for each fully developed flow. Long evolution times are necessary to relax transients in the computations; near bifurcations the mean transient lifetime can be very large.

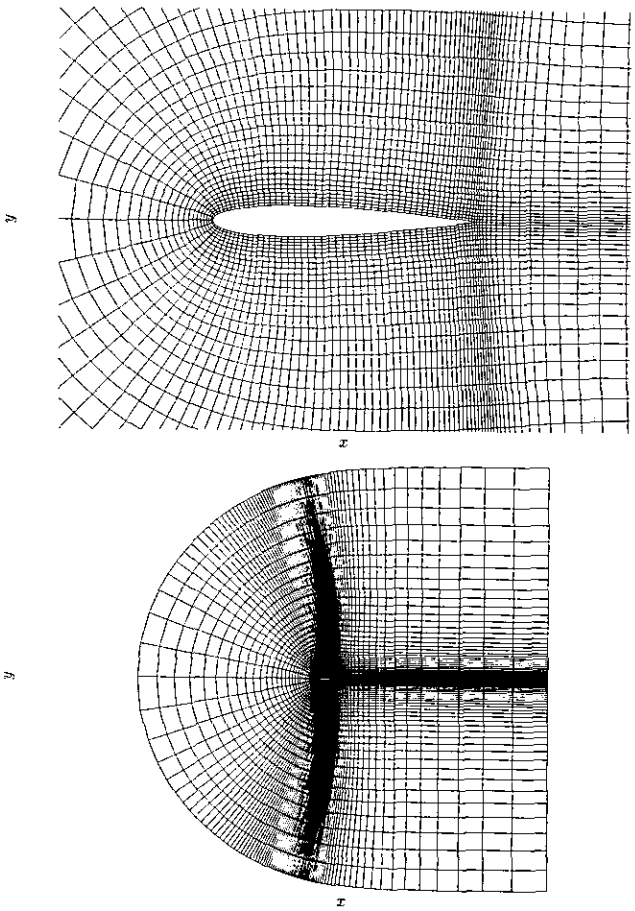

FIG. 1. Two views of the mesh topology of grid **A**.

III. OBSERVED BIFURCATION SEQUENCE

The largest number of trials was conducted on grid **A**. In this section, the various observed states and the overall structure of the bifurcation sequence for grid **A** will be presented and explained. The observed bifurcation diagram is shown in Fig. 2. The bifurcation parameter is the

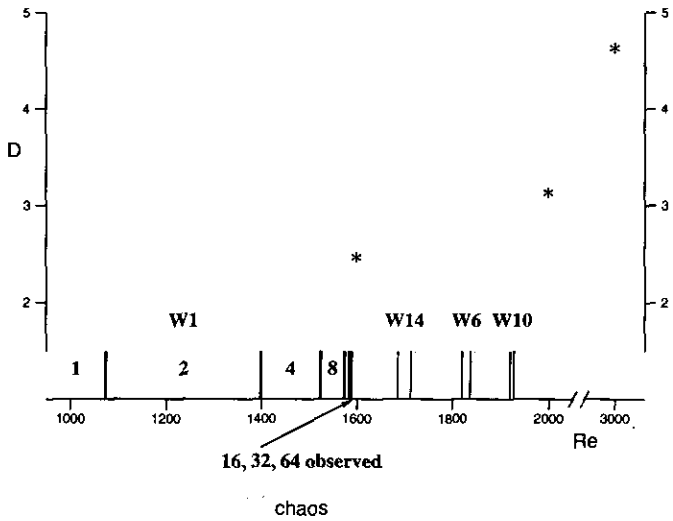

FIG. 2. The bifurcation sequence observed as Reynolds number is varied for the model system. The base periodic state is labelled 1, and the subharmonic states are labelled by the number of fundamental periods required.

Reynolds number of the flow. At the high angle of attack used here, flow over the model airfoil is unsteady at all Reynolds numbers; thus, the simplest observable behavior is periodic. The system apparently makes a transition from periodic behavior to chaos via a period-doubling cascade. After the first occurrence of chaos, windows of periodic behavior reappear for some range of Reynolds numbers, until finally a regime in which no periodic states have been found is reached. Trials at fixed Reynolds number and varying angles of attack indicated that the same bifurcation scenario, i.e., period-doubling, occurs as the angle of attack is increased. The method used to obtain the bifurcation diagram mimics experiment: at a low value of Reynolds number the flow is evolved until it reaches an asymptotic state, and then the Reynolds number is increased or decreased in small steps. At each step, the flow is again evolved until the asymptotic behavior appears. For this grid and the standard time step, no hysteresis was observed at any Reynolds number.

The development of the flow at Re = 800 from free stream initial conditions is depicted in Fig. 3. First, boundary layers grow on the upper and lower surfaces of the airfoil. A trailing edge starting vortex is shed and the upper surface boundary layer eventually grows to a significant height and separates. Vortices are now generated in the free shear layer. A vortex shedding process commences: as the large scale vortex structures pass over the upper surface at the trailing edge, an image vortex is shed at the trailing edge. The shed vortices are convected downstream, and the process repeats. At this Reynolds number the shedding process is periodic.

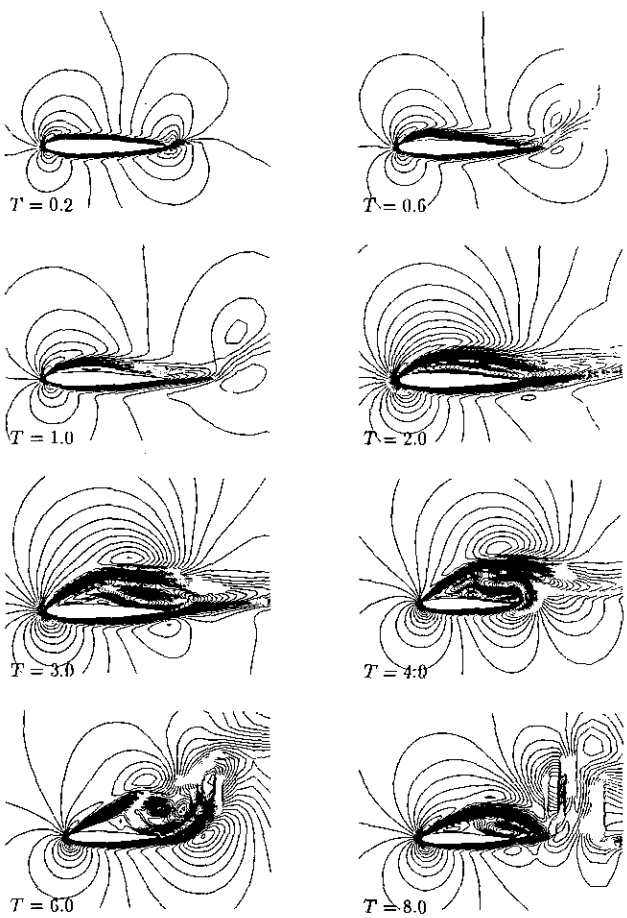

FIG. 3. Mach contours at selected times in the initial development of the flow for Re = 800.

In the language of dynamical systems theory, the periodic behavior for Re = 800 implies that the system has relaxed to a limit cycle or periodic attractor. Various aspects of the motion on this attractor are illustrated in Fig. 4, using a time series of the vertical component of velocity at a point near the trailing edge of the airfoil. Our presentation of the observed states will concentrate on the attractors found using this local quantity. The physical location will remained fixed for a particular grid and the range of Re studied. In the case of differing grids the physical location of the sample point is chosen consistently. If the flowfield is sampled at very distant spatial points or at inappropriate angles to the airfoil the velocity fluctuations become unobservably small. The spatial dependency of the observable dynamics is an interesting study in itself, beyond the scope of this paper, and is currently being investigated. Time series of a spatially averaged quantity, the coefficient of lift for the flow past the airfoil, display the same basic bifurcation sequence as does the local measurement used here, although an extensive analysis in the chaotic regimes has not been performed using this variable.

A portion of the velocity time series for Re = 800 is shown in Fig. 4a. A power spectrum obtained from a longer time series is given in Fig. 4b. The peak at $f_0 = 0.0046$ corresponds to the fundamental frequency of the single period shedding. In Fig. 4c the attractor is illustrated using the method of time delay reconstruction. This now-standard technique allows the reconstitution of full phase space behavior from scalar time series observations: given a time series of a scalar observable $v(t)$, the reconstructed vector observable is $(v(t), v(t+\tau), ..., v(t+(m-1)\tau))$. If the system attractor in the original full phase space is n-dimensional, then the m-dimensional reconstructed attractor will have the same invariant properties, e.g., fractal dimensions or Lyapunov exponents, for all m over a minimum value that is not greater than $2n+1$ [12]. In practice, if the dimension of the original attractor is not known, the reconstruction dimension is increased until the estimates of those invariant properties cease to change. The illustrations of reconstructed attractors in this paper will be two-dimensional, but for computational purposes higher reconstructions are necessary. The time delay for all of the reconstructions presented here was about one quarter of the mean orbital period.

The periodic behavior at Re = 800 gives way to a period-doubled state as the Reynolds number is increased. Time

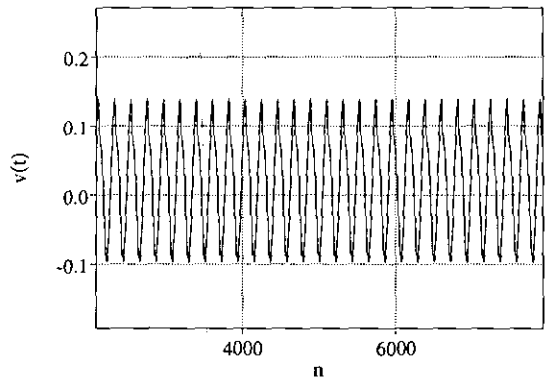

a) Time Series

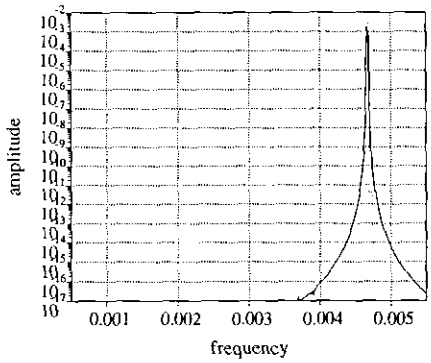

b) Frequency

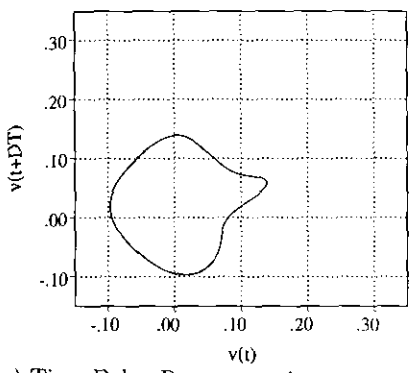

c) Time Delay Reconstruction

FIG. 4. Results for Re = 800.

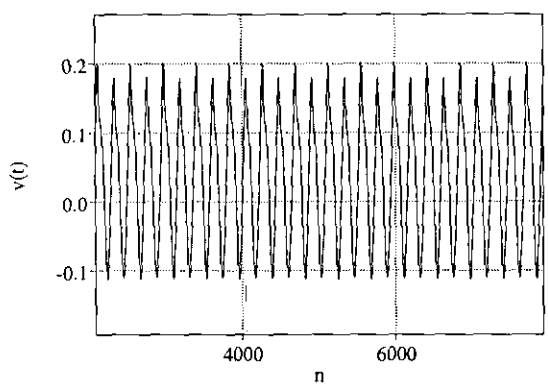

a) Time Series

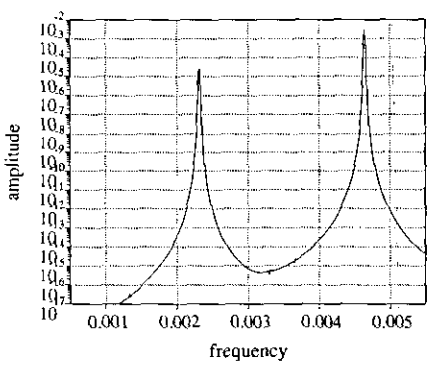

b) Frequency

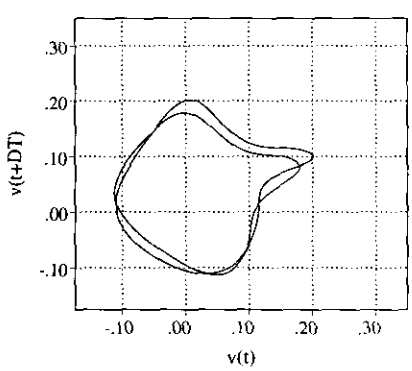

c) Time Delay Reconstruction

FIG. 5. Results for Re = 1075.

series data are used in Fig. 5 to illustrate the period-doubled flow at Re = 1075. The subharmonic nature of the bifurcation is evident in the time series (Fig. 5a) and in the power spectrum (Fig. 5b) a second peak appears at a frequency exactly half of the fundamental frequency. The apparent crossing of trajectories in the attractor reconstruction (Fig. 5c) is not real: in a three-dimensional reconstruction the simple two-loop attractor remains and the loops are separated.

The physical significance of the bifurcation is that the shed vortices become alternately more and less intense than the vortices shed in the periodic case. The physical mechanism that causes this behavior will be examined in some detail in Section V.

As the Reynolds number is increased further, a series of period-doubling bifurcations occur. The numerical evidence indicates that this sequence is part of a period-doubling cascade culminating in low-dimensional chaos. Power spectra for period 4 through period 32 states are shown in Fig. 6. The subharmonic adding of frequencies is clearly apparent. The principle characteristics of a period-doubling cascade are a geometric decrease in parameter window width for 2^n-periodic behavior as n increases, and also the culmination of the cascade in a transition to chaos, past an accumulation point at which n goes to infinity. Both of these properties are essentially impossible to prove numerically, but the collected evidence is convincing. While the precise locations of the observed period-doubling bifurcations have not been determined, it is clear from Fig. 2 that the periodic window widths decrease rapidly. The numerical evidence suggests a continued geometric decrease in window width after the period-64 window, with an accumulation point between Re = 1580 and Re = 1583.

Feigenbaum [13] discovered that a universal geometric scaling factor exists for the window widths in period-doubling cascades of unimodal one-dimensional maps, in the limit as the period goes to infinity. This "Feigenbaum number" is approximately 4.67. In our system, the limiting scaling factor for the observed windows is about 4.5, with a large amount of uncertainty. The scaling factor in the limit

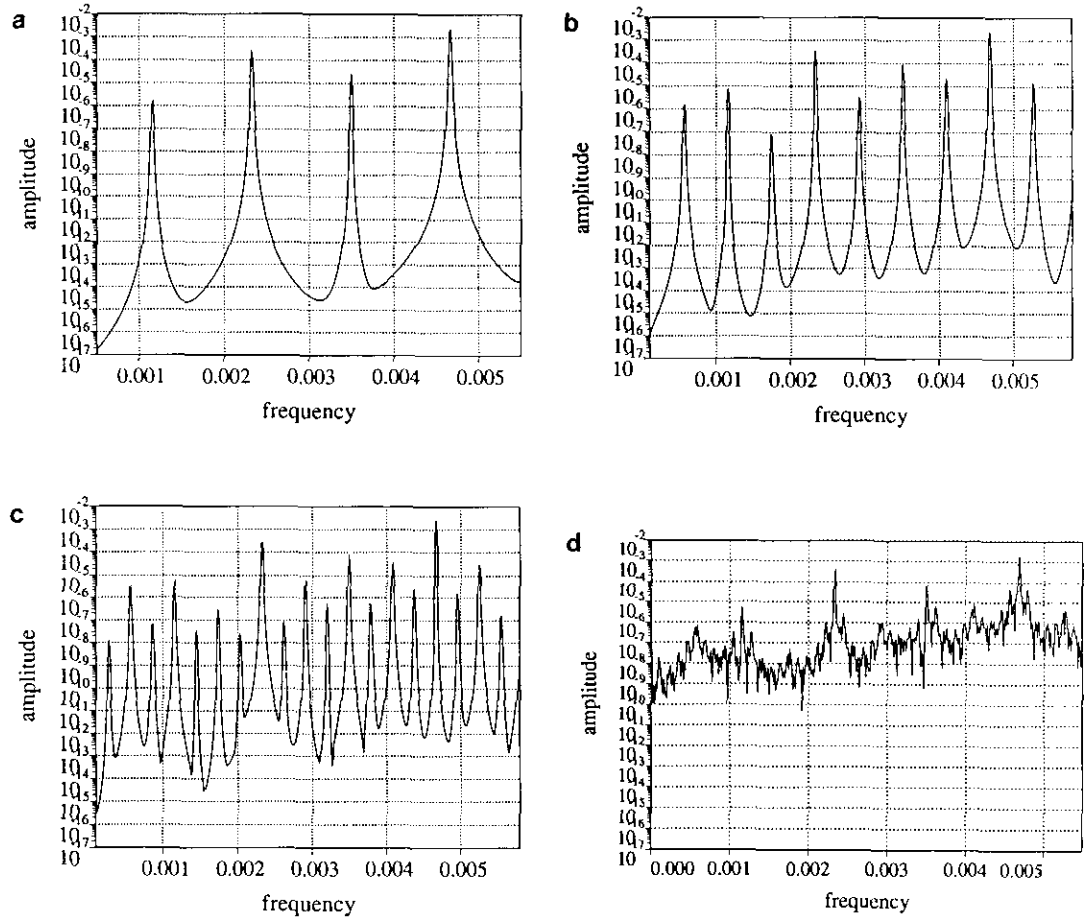

FIG. 6. Power spectra for periodic states in the period-doubling cascade: (a) Re = 1400, periodic 4; (b) Re = 1525, period 8; (c) Re = 1575, period 16; and (d) Re = 1580, period 32.

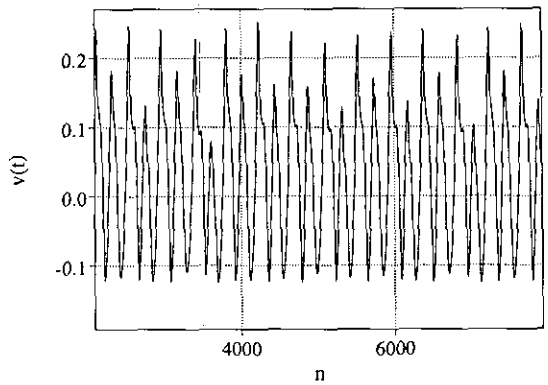

a) Time Series

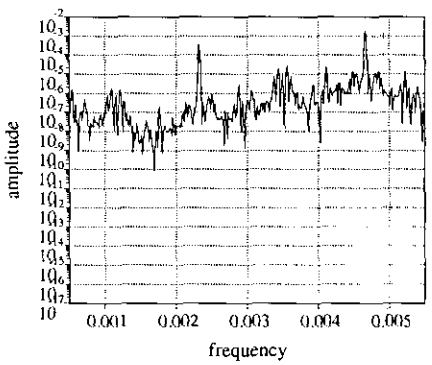

b) Frequency

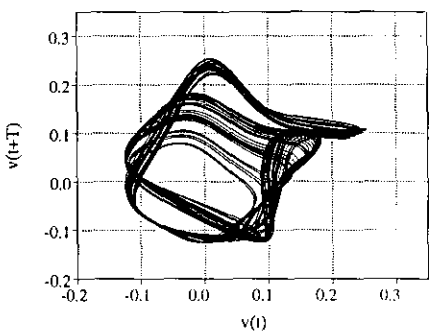

c) Time Delay Reconstruction

FIG. 7. Results for Re = 1600.

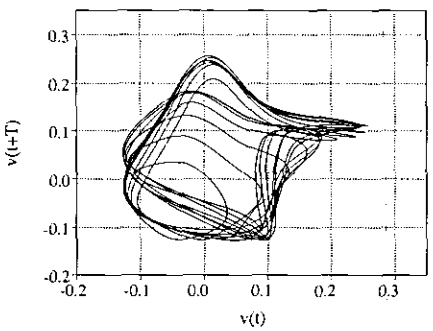

a) $Re = 1695$

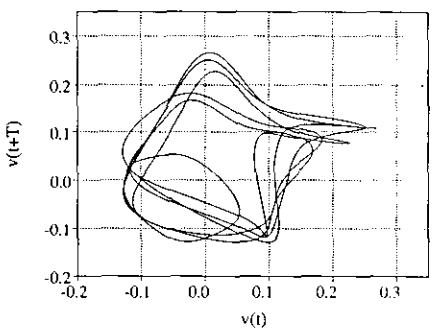

b) $Re = 1825$

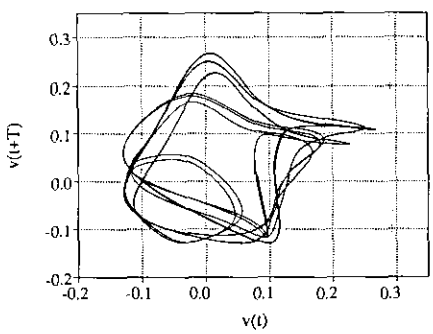

c) $Re = 1832$

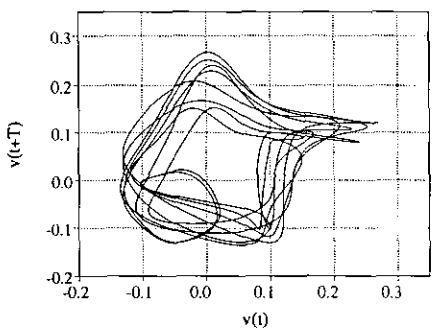

d) $Re = 1940$

FIG. 8. Time delay reconstructions.

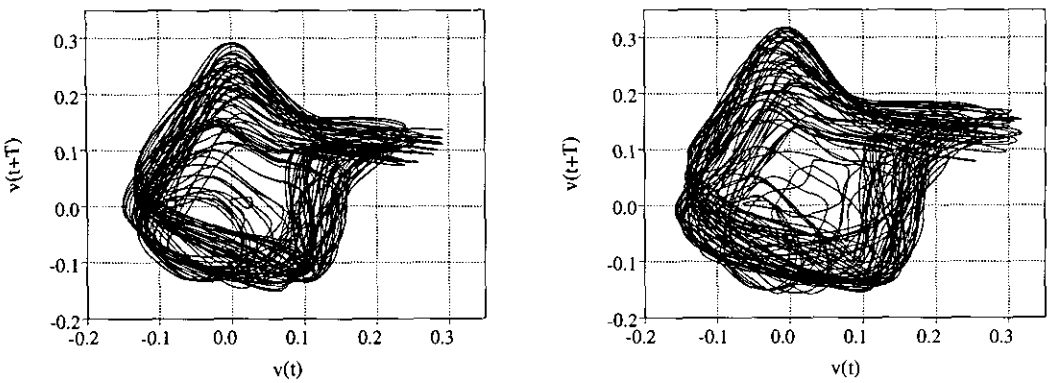

a) $Re = 2000$ b) $Re = 3000$

FIG. 9. Time delay reconstructions.

of infinite-period flow may converge to the Feigenbaum number, but this would be extremely expensive to verify.

The longest period observed so far is the period-64 behavior. One period of evolution in this regime requires approximately 2500 cpu s on a Cray-XMP and the analysis requires multiple orbits for good information extraction (on the order of 10 orbits seems sufficient). Higher periodic states would require too much time to be worthwhile, even if well-relaxed initial conditions were in hand. As a period-doubling bifurcation is approached, the average relaxation time for transients diverges like the inverse square root of the distance from the bifurcation. In the high-period windows, no parameter setting is far from a bifurcation point, and the relaxation times can become enormous. Nevertheless, the sequence of observed states and the rapid decrease in the corresponding parameter window widths are convincing evidence for a period-doubling cascade.

The cascade should end at a period-doubling accumulation point, followed by (low-dimensional) chaotic behavior. At Re = 1600 (depicted in Fig. 7), the system evolution is aperiodic. The power spectrum has a broadband component well above the computational noise floor, and the

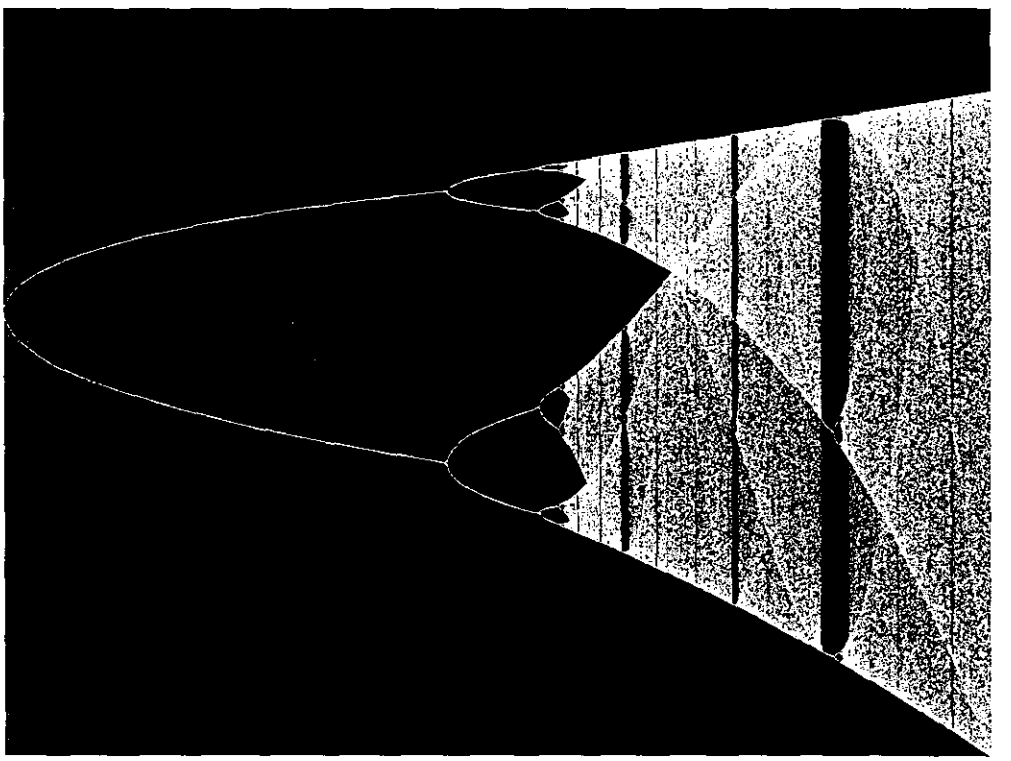

FIG. 10. Logistic map $z^{n+1} = Rz^n(1 - z^n)$ for $R = 3.0$–4.0.

banded structure typical of chaotic attractors is apparent in the time delay reconstruction. This case was run for an extremely long time (on the order of 300,000 time steps): this is not a transient, but is the asymptotic state. In the next section of this paper it will be established that the Re = 1600 behavior is low-dimensional chaos.

The system response for Reynolds numbers between 1600 and 3000 is diagrammed in Figs. 8 and 9: a series of chaotic states interspersed with periodic windows. The periodic windows appear abruptly from chaos as the Reynolds number is increased, although there is some concentration of the chaotic probability distribution just prior to the transition. All of the periodic windows that have been studied in detail show a period-doubling return to chaos. Past Re = 1600, the system state is chaotic up to about Re = 1695, where a period-14 window of behavior (Fig. 8a) appears. This window ends in a period-doubling bifurcation to a period-28 state at around Re = 1706, and several successive period doublings are observed before chaos returns around Re = 1715. The chaotic behavior after Re = 1715 is similar to that seen at Re = 1600. Another periodic window with a period-6 base state (Fig. 8b) begins at about Re = 1825. It also undergoes a period-doubling cascade back to chaos. The period-12 state at Re = 1832 is shown in Fig. 8c. Other periodic windows are seen as the Reynolds number is increased further; e.g., a period-10 window begins around Re = 1940, see Fig. 8d. Eventually, however, periodic windows cease to appear. The nature of the chaotic behavior changes as well. At Re = 2000, in Fig. 9a, the chaos is still somewhat similar to that seen at Re = 1600, but at Re = 3000 (Fig. 9b) the chaos is higher-dimensional, as will be shown below.

Putting aside for a moment the dimensionality of the chaotic states, the bifurcation scenario described above is a familiar one. Simple low-dimensional maps, such as the logistic or Hénon maps, also display an initial period-doubling cascade to chaos followed by windows of periodicity embedded in chaos. Figure 10 shows part of the bifurcation sequence for the logistic map. There are an infinite number of periodic windows for the logistic map; if this is the case in the model system, one can only hope to discover the largest of them given the limits of computer resources. Interestingly, the largest periodic windows in the logistic map prior to the period-three window are of periods 14, 6, and 10, just as was found in the airfoil simulations. Another similarity between the logistic map bifurcation structure and the airfoil simulations is the banded nature of the chaotic attractors. For the logistic map, note the merg-

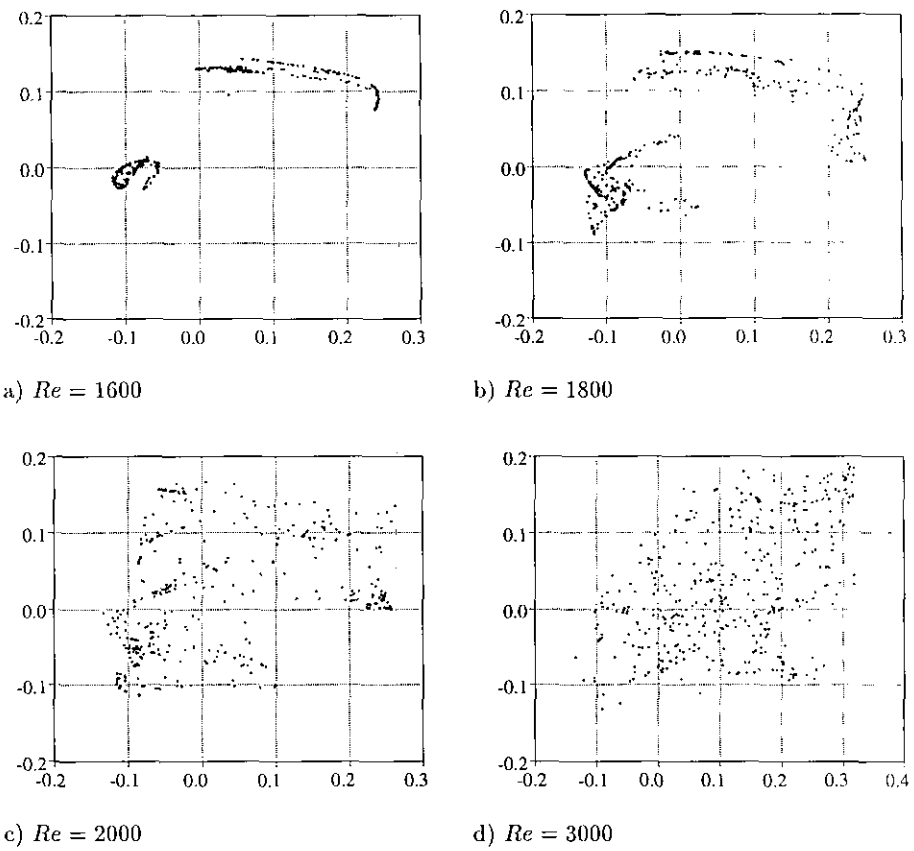

FIG. 11. Poincaré sections.

ing of the two chaotic bands at about $R = 3.67$ that allows stable odd-period orbits to appear. Figure 11 is a set of Poincaré sections for three chaotic states in the airfoil simulations at increasing values of Reynolds number. The sections were obtained by finding the intersections with a transverse plane for a three-dimensional reconstruction of each attractor. At Re = 1600, two distinct chaotic bands are present, and intersections occur alternately between the right and left bands of the section. The two bands are approaching one another at Re = 1800 and merge before Re = 2000. Finally, the Re = 3000 result shows a more uniform distribution of intersections. The merging of the two bands would allow the appearance of odd-period windows, but these have not been observed. Small windows may exist, but past Re = 2000 the chaos in the system begins to become higher-dimensional, making a transition back to periodicity more and more unlikely. It is not yet possible to say whether the merging of the two chaotic bands directly signals the onset of higher-dimensional chaos. It has not been possible to extract a plausible one-dimensional map from the observed low-dimensional chaos, and no direct link has been established between the logistic map and the airfoil flow. However, the similarity between the two bifurcation sequences is evidence suggesting that some relatively simple mechanism is responsible for the transition to chaos in the airfoil simulations.

IV. MESH REFINEMENT, ALGORITHM PARAMETER STUDIES

The numerical solutions presented above are at best approximate solutions of the Navier–Stokes equations. The authors know of no experimental data to support the results, although there have been other similar computational results by Fortin *et al.* [8] and Ghia *et al.* [9]. To be confident that the inaccuracies and approximations of the numerical simulation do not lead to inconsistencies with the real physics of the fluid flow, it is necessary to test the effect of varying the numerical model. This includes studies with different spatial and temporal resolution as well as studies in which the spatial and temporal differencing schemes are varied.

Mesh refinement studies were performed using grids **A**, **B**, and **C**. The results on the finer grids (**B** and **C**) are not quite as extensive due the exhaustive computation time required. Typically on the order of a 100,000 iterations are needed to get good samples for the above analysis. Figure 12 shows time-delay reconstructed phase diagrams for grid **B** solutions at various values of Reynolds number. For this grid the first period doubling takes place around Re = 1100, which is similar to the location of this transition for the coarser grid **A** case. In contrast, the second period doubling for grid **B** occurs at Re $\approx$ 2600, by which time the grid **A** bifurcation sequence has completed the cascade to chaos. At Re = 2800 the grid **B** simulation displays either high-order periodic or weakly chaotic behavior leading to the definite chaotic result for Re = 3000. The results are strong evidence that the period-doubling cascade observed with the coarser mesh are still present, although the location of the period-doubling accumulation point and the transition to chaos has been shifted to higher Reynolds numbers. Limited results for the finest mesh, **C** again show a period-2 solution is near Re = 1100 and chaos for Re = 3000. The structure of the flow is more complicated for grid **C**, as shown in Fig. 13. This mesh captures more downstream structure of the shed vortices and one even sees pairings of the vortices. Figure 13d shows, for comparison, a coarse grid **A** result, where the downstream flow is unresolved and washes out the shed vortices. These results establish that the basic physical process which gives rise to period doubling in the system is present over a wide range in mesh fineness and that the mechanism does not involve vortex interactions far from the airfoil. It seems very likely that a complete period-doubling cascade occurs for all of these meshes as well. The detailed study needed to find the bifurcation points for more of the cascade in the finer meshes would be extremely expensive in terms of computer resources and thus has not been performed.

Besides mesh refinement, there are other tests of accuracy and consistency which can be performed. Recall that the sharp trailing edge of the airfoil necessitates the addition of artificial dissipation to stabilize the computations. The values are kept as low as possible and a study was performed, where the coefficients were increased and decreased. At the lowest values possible and for typical values suggested in papers on the subject [11], the result was a shifting of the period-doubling Reynolds numbers, but the sequence of doublings to chaos still exists. At large values the resulting flows were damped and in the extreme cases the unsteadiness was completely suppressed, although these represent unreasonable values.

Results from upwind, TVD algorithms have also been obtained with qualitatively similar solutions. Results from a third-order accurate upwind based Roe Riemann solver scheme are shown in Fig. 14 for grid **A** and the $M_\infty = 0.2$, $\alpha = 20°$ conditions. Single period shedding persists to a higher Reynolds number (up to Re $\approx$ 1800) with this numerical model than was observed with ARC2D at the same parameters. A fuzzy period-2 result is seen at Re = 2000, with a more transient looking result at Re = 2100, and a chaotic result at Re = 2200. Results at higher Reynolds numbers are definitely chaotic. The artificial dissipation of this scheme is tied in with the nature of the upwind differencing and, although it is less dissipative than, for instance, a first-order scheme, the amount of dissipation does influence the results. In fact, a first-order upwind result would completely suppress the unsteadiness

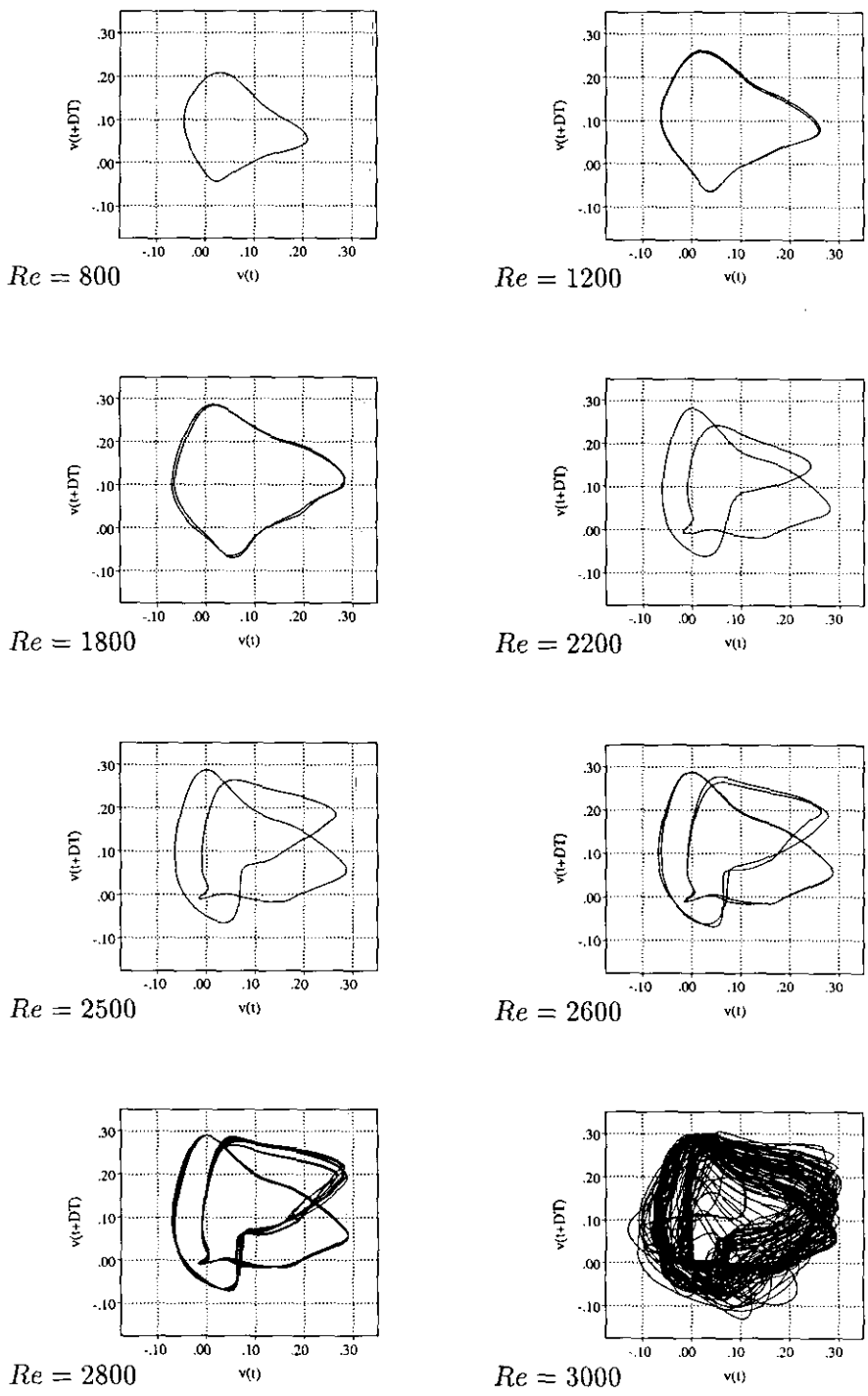

FIG. 12. Time delay reconstructions at selected Reynolds numbers for grid **B**.

and produce a fixed-point solution. Various schemes of this sort are possible, but the basic result is that the more dissipative forms (upwinding produces inherent artificial dissipation due to truncation error), produce similar results to the large artificial dissipation results mentioned above. For the low dissipation methods, the results are similar to the unsteady sequence described above, i.e., a sequence of period doublings cascading to chaotic results at high Reynolds numbers.

Time accuracy has been evaluated by comparing first-, second-, and third-order results for selected cases. The time step was also halved, quartered, and doubled to assess the

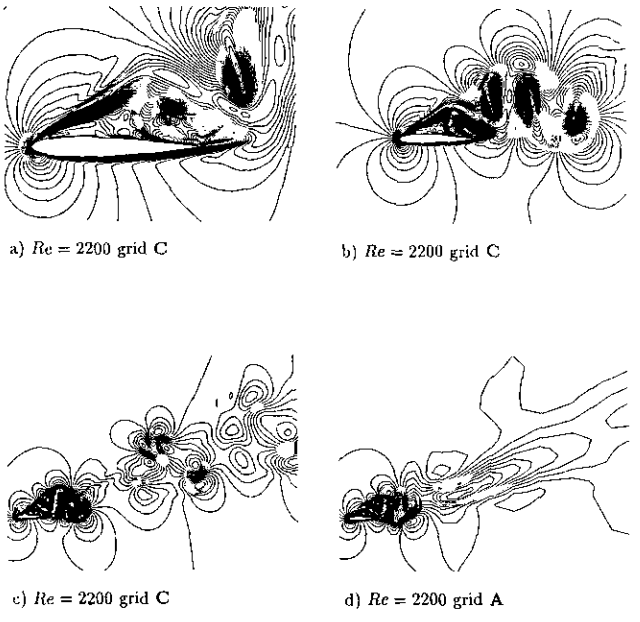

FIG. 13. Mach contours at selected Reynolds numbers for grid C.

time accuracy required. At the time step used here, all the results were consistent across different time accuracies. Most of the results shown were obtained using first-order time accuracy, since that option requires the least amount of CPU time per step.

The tests of resolution and other parameters present strong evidence that the chaos observed in these numerical simulations is also present in the true, exact solutions of the underlying equations of motion. It is not possible to completely eliminate the possibility that the chaos is numerically generated, however, and it is therefore important to understand how a numerical method can cause spurious choas to appear. The simple model problem presented in the Appendix indicates that numerically generated "spurious" behavior can occur when numerical methods are pushed past their linear stability bounds. In fact, if the bifurcation that gives rise to the spurious solution is subcritical, such a solution can be observed somewhat below the linear stability bound. While there is no direct evidence that numerical solution of the Navier–Stokes equations suffer from the same instabilities, this possibility must be con-

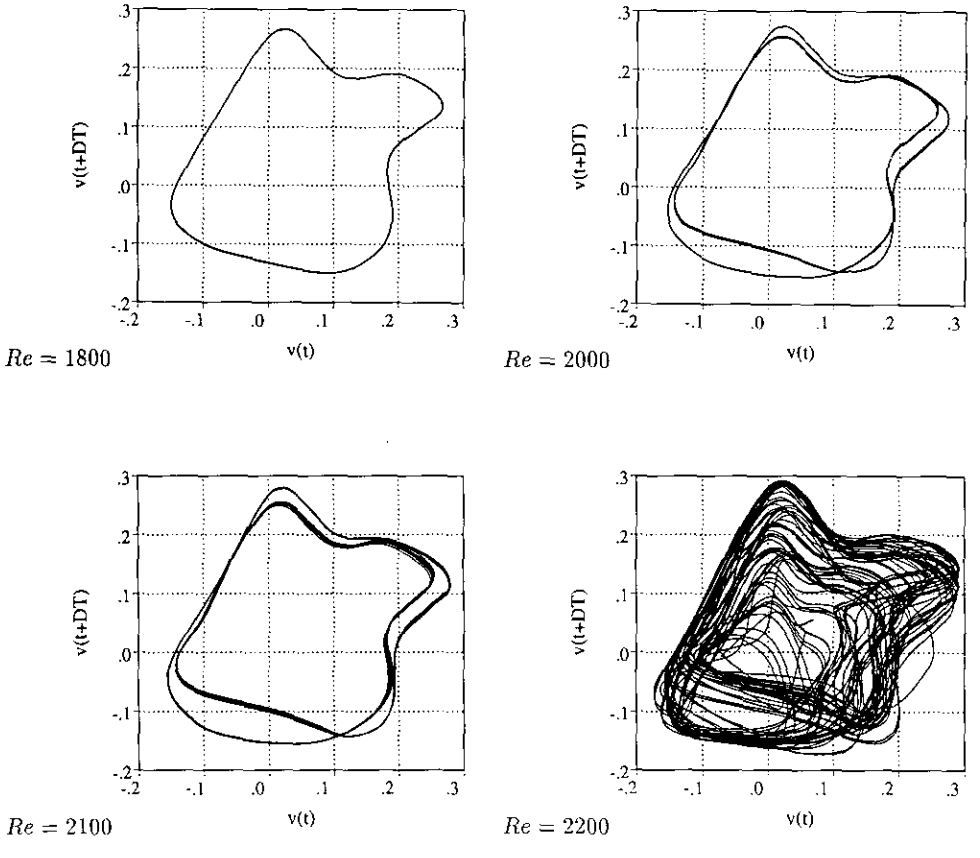

FIG. 14. Time delay reconstructions at selected Reynolds numbers for a third-order upwind scheme.

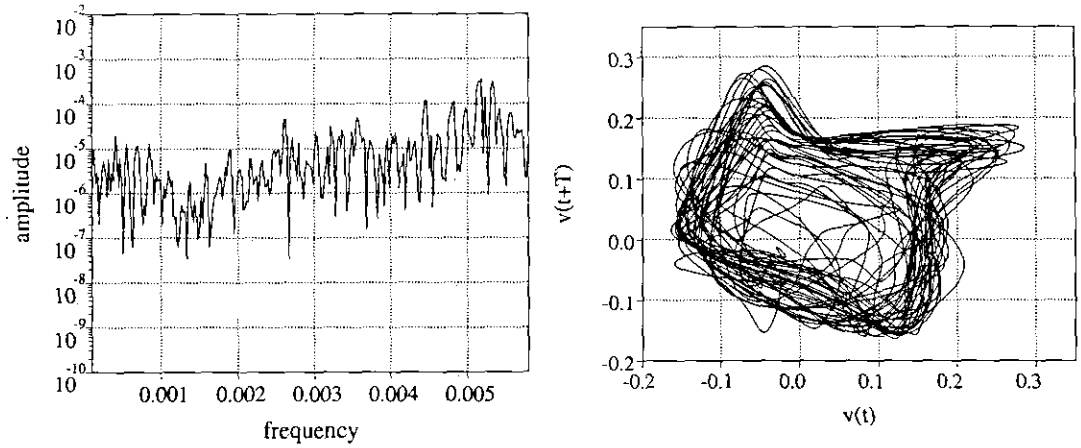

FIG. 15. RK3 frequency decomposition and time delay reconstruction Re = 3000.

sidered. To test the airfoil results, a numerical experiment was performed using a third-order Runge–Kutta (RK3) time integration. For RK3 the linear stability bound corresponds to a CFL number of 2.5175 for the above ODE, Eq. (2), and the bifurcation boundary coincides with the linear stability boundary. Computations were performed using a CFL number of 1.75, well below this limit, for the Re = 3000 case. In this case the number of iterations required is increased by a factor of 10 and therefore a complete description of the results is not possible. Figure 15 shows the time delay reconstruction and frequency decomposition for the RK3 method which is similar to the previous Re = 3000 results. The fundamental frequency, $f_0 = 0.005$, compares well with the larger time step, implicit algorithm data. Results from the standard code at the same time step used for the RK3 integration compared even better. The results remain chaotic and similar to the large time step data supporting the conclusion that the cascade to chaos is not driven by the numerical discretization.

V. ANALYSIS OF CHAOS

The numerical evidence presented in the previous sections indicates that a sequence of bifurcations culminating in a period-doubling cascade takes the model system from unsteady but periodic behavior to chaos. While the details of this bifurcation sequence are affected by the choice of numerical model, the same basic route is shown to exist over a wide range of parameterizations. Assuming then that the chaos is a real feature of the two-dimensional flow in this Reynolds number regime, the next step is to characterize the chaotic flows using some standard tools from nonlinear dynamics. This analysis will be restricted to the coarse grid cases presented in Figs. 4 through 11. The Re = 3000 aperiodic behavior is clearly more disordered than the Re = 1600 or 2000 cases. This distinction can be made more quantitative by obtaining fractal dimension estimates and partial Lyapunov exponent spectra for these flows. The Lyapunov exponents, which will be described in some detail below, can be estimated either from time series data or by solving an augmented set of equations for the time advancement of the system. Given sufficient computer resources, the latter approach will yield more accurate estimates. Of course, experimentalists are limited to the data sets they have in hand, and even if the flow can be solved for numerically, the expense may be prohibitive. For purposes of comparison, therefore, both approaches will be tested here.

The Lyapunov exponent spectrum of an attractor is perhaps the most complete characterization possible of the geometric properties of an attractor and the dynamical properties of a flow on that attractor. The Lyapunov exponents $\{\lambda_i\}$ measure the long-time average exponential growth or decay of infinitesimal perturbations to a phase space trajectory. The number of Lyapunov exponents thus equals the number of independent phase space directions: an attractor in an N-dimensional phase space has N Lyapunov exponents, while an attractor for a system governed by partial differential equations has an infinite number of Lyapunov exponents. Negative Lyapunov exponents correspond to the decay of perturbations towards the attractor. If an attractor has a positive Lyapunov exponent, perturbations on the attractor can grow exponentially fast in the long term, and the attractor is defined to be chaotic. The Lyapunov exponents are ordered so that $\lambda_1 \geq \lambda_2 \geq \cdots$, i.e., from largest to smallest. The signs of the exponents can be used as a classification scheme for the attractor: all negative exponents implies a fixed point attractor, $\lambda_1 = 0$ and all others negative imply a limit cycle (periodic orbit), and $\lambda_1 > 0$ implies chaos. Note that this classification does not distinguish between periodic flows of different periodicity or between different chaotic flows. The magnitudes of the Lyapunov exponents and the number of positive exponents give more detailed information. A positive

Lyapunov exponent indicates that there is a direction *on the attractor* such that perturbations in that direction will grow exponentially. The unavoidable uncertainty in a measurement of the system state will thus spread exponentially rapidly. Even though the flow is confined to a region of phase space (the attractor), it is not possible to predict the system state with any certainty at arbitrary future times (except to say that it is on the attractor). The more positive Lyapunov exponents there are, the more directions of instability on the attractor exist, and thus the higher the fractal dimension of the attractor becomes. This relation can be made quantitative: the Kaplan–Yorke [14] conjecture relates the Lyapunov exponent spectrum to the dimension of the attractor:

$$D_\lambda = m + \left(\frac{\sum_{i=1}^{m} \lambda_i}{|\lambda_{m+1}|} \right),$$

where m is the largest number for which $\sum_{i=1}^{m} \lambda_i$ is positive. The fractal dimension can also be estimated directly from time series data via a number of algorithms, e.g., the Grassberger–Procaccia technique [15].

It is important to note the difference between the long-time average Lyapunov exponent, λ_i, and the short-time contribution to that average at some time t, $\lambda_i(t)$. For simplicity's sake, consider only the largest Lyapunov exponent, λ_1. While λ_1 may be positive, $\lambda_1(t)$ can be positive or negative and, in fact, the range of short-time contributions is very large. Large positive or negative maxima in the short-time contributions to a positive Lyapunov exponent mark important moments in the evolution of the flow. Furthermore, it can be shown [5] that the form of the perturbation corresponding to λ_1 at any given instant of time t is unique and depends only on the phase space location of the fiducial trajectory at that time. The orientation of a randomly chosen perturbation introduced at some earlier time will approach this unique form exponentially rapidly. By studying the short-time contributions to locate the important times and then studying the form of the unique perturbation corresponding to λ_1 at those times, it may be possible to discover the physical instabilities driving the flow. Vastano and Moser [5] have used this technique to show that the transition to chaos in a closed flow system, Taylor–Couette flow, is driven by a Kelvin–Helmholtz instability of the azimuthal jet at the outflow boundary between the large-scale Taylor vortices present in the flow.

All of the techniques for estimating the Lyapunov exponents of an attractor involve following the evolution of perturbations to some fiducial phase space trajectory on the attractor. The simplest implementation assumes no knowledge of the attractor beyond time series measurements of the system state (see Wolf *et al.* [16] for details). The method of time delays previously discussed is first used to obtain a full phase space reconstruction of the attractor. Now to estimate λ_1, follow a fiducial trajectory and use a neighbor of the first point on the trajectory to define an initial separation. Evolve both points by stepping through the time series. The separation must remain small enough to be considered effectively infinitesimal. When the separation grows too large (which it will if the attractor is chaotic), replace the second data point with a new point, chosen to maintain the orientation of the separation, but reducing its length. The long-time average exponential growth rate of the separation is an estimate of λ_1. To estimate the first two Lyapunov exponents, follow the evolution of the fiducial point and two other points defining an small area, which will grow at the long-time average exponential rate of $\lambda_1 + \lambda_2$. This method could be extended to calculate more exponents, but the requirements for replacement points become increasingly expensive to evaluate. Since all of the perturbations are defined by actual data points, large time series covering many fundamental periods of oscillation may be necessary to obtain accurate Lyapunov exponent estimates.

This technique was applied to time series data from each of the chaotic flows studied here. Typically, a four- or five-dimensional reconstruction of the attractor was used. The variable parameters of the technique are the number of data points used, the evolution time step for the perturbations, and the length scale used. Extensive trials were made to find the most probable value for the Lyapunov exponents in each case. An independent technique (using the Grassberger–Procaccia [15] algorithm) was applied to the data sets to estimate the dimension for each attractor. For the $\mathrm{Re} = 1600$ attractor a time series of 210,000 points was used. It was found that $\lambda_1 = 0.30$ bits/orbit and $\lambda_2 = 0$ to within the uncertainty of the estimate. The dimension of this attractor was estimated to be 2.25, using the same data set. The Kaplan–Yorke conjecture would place a lower bound of 2.0 on the attractor dimension in this case, so the Lyapunov exponent estimates are compatible with the dimension estimate.

For the $\mathrm{Re} = 2000$ attractor, the estimate of λ_1 rose to 1.08 bits/orbit, while again λ_2 was indistinguishable from zero. A data set of 160,000 points was used here. The estimated dimension of the attractor was 2.4, again in general agreement with the Lyapunov exponents. For $\mathrm{Re} = 3000$, the highest value tested in detail, 148,000 points were used to obtain estimates of $\lambda_1 = 1.2$ bits/orbit and λ_2 apparently slightly positive but too close to zero to be quantified. The dimension estimate for this data set rose to 3.4. If there are two positive exponents, then the Kaplan–Yorke formula sets the attractor dimension at no less than 3.0, so again the Lyapunov exponent estimates agree with the dimension estimate.

If the equations of motion for the system are known and solvable, either analytically or numerically, then as many

Lyapunov exponents as desired may be estimated by solving the full set of equations for the fiducial trajectory and simultaneously evolving a set of N perturbations to estimate N Lyapunov exponents. Ideally, the perturbations should be infinitesimal and thus evolve according to the linearized equations of motion about the fiducial trajectory. Unfortunately, it is not always convenient numerically to obtain the linearized equations of motion. Due to the conservative formulation used in ARC2D and the triplet nature of some terms, such as the convection of momentum, the perturbation form of the equations is difficult and lengthy to form. Instead, it is simpler to use the flow solver as a functional operator, passing various solutions through it, so that all functional attributes of the flow solver (e.g., boundary conditions) can be brought to bear. In such cases, the fiducial trajectory and a set of N perturbed trajectories are evolved, all with the full nonlinear equations. The perturbations are then found at any time by subtracting the fiducial state vector from each perturbed state. As was noted earlier, the volume spanned by the first k Lyapunov perturbations grows like the sum of the first k Lyapunov exponents. A computational difficulty arises because all of the individual Lyapunov perturbations will collapse towards the unique direction corresponding to λ_1. To avoid this problem, the perturbation vectors are periodically Gram–Schmidt reorthogonalized. This procedure alters the perturbations but does not affect the orientation of the volume spanned by the first k perturbations for all k. Therefore, the volume will continue to grow at the correct rate. Also at this time the perturbations are re-normalized to their initial amplitudes. See Vastano and Moser [5] for details. When finite amplitude perturbations are used, it is essential to test the effect of perturbation amplitude on the Lyapunov exponent estimates. If the perturbations are small enough to be effectively infinitesimal, then halving the amplitude will not change the estimates.

In the computations performed here we have analyzed the Re = 1600, 2000, and 3000 cases. Random perturbations of the base state are used to initialize the perturbed fields and amplitudes on the order of 10^{-8} based on order 1 flowfield quantities were sufficiently small. Long term average λ_i are given for the Re = 1600, 2000, and 3000 in Figs. 16a–c. In all three cases there is one positive Lyapunov exponent, one zero exponent (to acceptable accuracy), and finally negative values. Table I shows λ_i for the various cases along with the fractal dimension D_λ. Note that the increase in D_λ is not due to additional positive Lyapunov exponents but is, instead, caused by a decrease in the magnitudes of the first few negative exponents.

The numerically obtained Lyapunov exponents presented

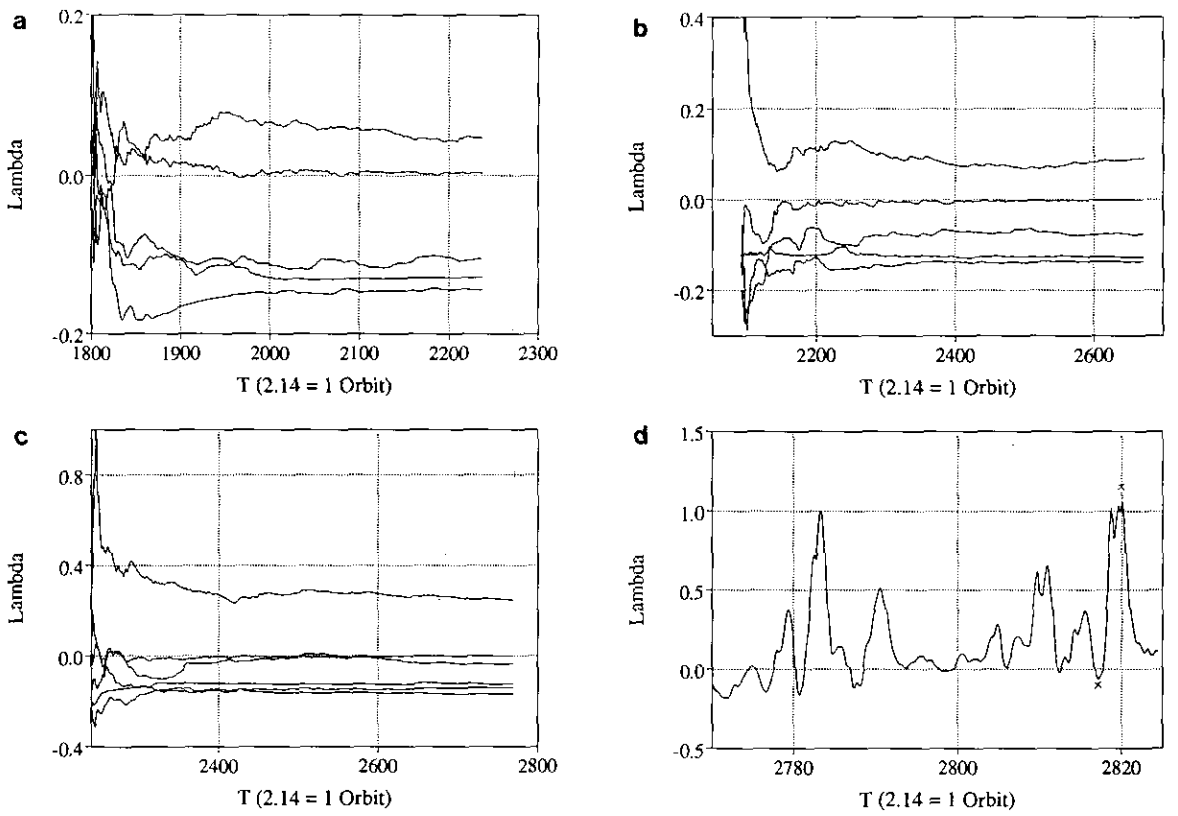

FIG. 16. (a) Re = 1600; (b) Re = 2000; (c) Re = 3000 long term λ_i; (d) short term contributions for Re = 3000.

TABLE I

Lyapunov Exponents from Perturbation Analysis

Lyapunov exponents and fractal dimension		
Re = 1600	Re = 2000	Re = 3000
+0.10067	+0.19348	+0.52650
+0.00678	−0.00321	−0.00073
−0.22545	−0.16266	−0.06946
−0.27604	−0.27182	−0.26022
−0.30910	−0.29130	−0.30011
−0.34065	−0.33226	−0.36016
D_λ	D_λ	D_λ
2.48	3.10	4.65

in Table I are qualitatively similar to the Lyapunov exponents previously obtained from the time series data. The trend of one positive Lyapunov exponent that increases with Reynolds number is observed in both sets of estimates. The actual values of the exponents are very different, however. This points out the difficulty in doing quantitative comparisons between different systems using experimentally obtained Lyapunov exponents. The numerically obtained values for the dimension are also somewhat higher than was indicated by the time series data. The trend of higher dimension with increasing Reynolds number is still evident and these results are considered definitive evidence that the solutions are chaotic.

The short-time contributions to the λ_i, in particular λ_1, and the corresponding perturbation fields contain information as to the events associated with the production of chaos. As an example, Fig. 17 shows contours of the perturbation field convective derivative of the metric norm used in the Gram–Schmidt process (dotted curve) and the vorticity field (solid curves). These are taken at the time of maximum short-time contribution to λ_1, the marked maximum in Fig. 16d. The convective derivative field is an order of magnitude stronger than the corresponding field at the minimum (also marked in Fig. 16d). While it is difficult to interpret this data, one sees that the perturbation field intensity is largest in between the two counterrotating vortices being shed by the body. These vortices are at their largest size at this time and at other times they are not interacting as strongly. This static picture indicates that the physical mechanism underlying the chaos (and likely the period-doubling cascade as well) is a vortex–vortex interaction in the immediate vicinity of the trailing edge of the airfoil and that interactions between the shear layer and the vortices or between downstream vortices do not play a significant role. Work is currently in progress to better analyze the spatiotemporal structure of the perturbation field density and its spatial and temporal derivatives in order to extract a clearer picture of the chaos-generating mechanism.

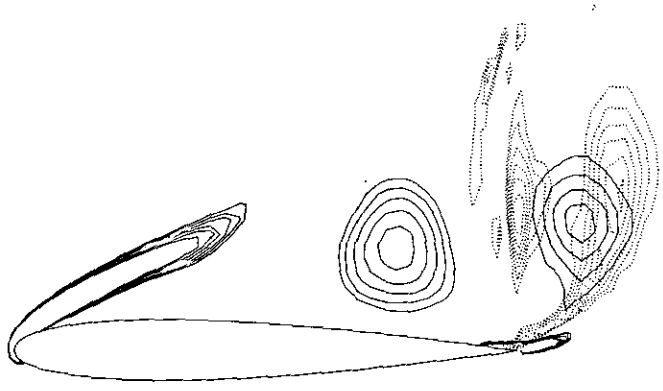

FIG. 17. Contours of vorticity (solid) and convective derivative of perturbation metric (dashed) for Re = 3000.

VI. SUMMARY

Numerical computations of two-dimensional flow past an airfoil at low Mach number, large angle of attack and low Reynolds number shows a sequence of flow states leading from single-period vortex shedding to chaos via the period-doubling mechanism. Analysis of the flow in terms of phase diagrams, Poincaré sections, and flowfield variables has been used to substantiate this result. Although the flow at any particular Reynolds number in the transition regime is sensitive to algorithm parameters (such as mesh refinement, artificial dissipation level, and differencing accuracy), the basic result of period doublings to chaos exists. A separate study, where the Reynolds number was fixed and the angle of attack used as the bifurcation parameter, showed a similar sequence of doublings to chaos. It should be stressed, that the authors by no means are suggesting that there is an equivalent physical flow. There is no experimental or theoretical evidence as to the physical realization of this type of flow. At best one can say that the numerical solution of the two-dimensional Navier–Stokes equations exhibits these mechanisms. At worst, we have a numerical computation, somewhat sensitive to numerical parameters, which shows a low-dimensional road to chaos.

High-dimensional chaos is easy to observe in fluid flows. Unfortunately, the current state of the art in nonlinear dynamics cannot contribute much new understanding of these flows. To make any progress, model systems must be found in which the transition to chaos is gradual, but in which high-dimensional behavior does appear. The system reported here is particularly encouraging: not only does it display the desired gradual transition, but it also acts for a significant range of Reynolds number as if it were governed by a one-dimensional map. Now the task is to discover why this behavior occurs and to see what implications this may have for the structure and dynamics of high-dimensional chaos in this and related systems.

APPENDIX: NUMERICALLY GENERATED CHAOS

Numerical experimentation only provides a limited analysis of the effects of numerics and computational error on the computed solutions of a system of equations. Typically, the numerical analyst relies on model problems, linear theory, and past experience as a guideline in assessing and using numerical methods. Linear theory, while useful, can sometimes fail to uncover all the interesting characteristics of a method applied to a nonlinear problem. Recent work (Prüfer [17] and Lorenz [18]) has shown that simple numerical solution techniques for a nonlinear ODE can produce the equivalent of a chaotic map such as the logistic map,

$$z^{n+1} = Rz^n(1 - z^n), \tag{1}$$

which for $3 \leqslant R \leqslant 4$ produces the asymptotic behavior of z as shown in Fig. 10. This figure was generated by iterating Eq. (1) from the initial value $z^0 = 0.25$ for 400 unplotted iterations and then plotting z^i for $401 \leqslant i \leqslant 600$. For $R = 3.0$ the asymptotic behavior is a fixed point, i.e., $z^{i+1} = z^i$. At $R = 3.0$, a period-doubling cascade to chaos begins, followed by a region of mixed chaotic and periodic states up to $R = 4.0$ past which z^i diverges to infinity, typically characterized as instability.

To see how such behavior can arise in a numerical solution to an ODE consider the simple ODE

$$y_t = y(1 - y), \qquad y(0) = y_0, \qquad 0 \leqslant y_0 \leqslant 1 \tag{2}$$

which has the well-behaved exact solution

$$y(t) = \frac{y_0}{y_0 + (1 - y_0)\, e^{-t}}. \tag{3}$$

A numerical solution may be obtained by applying Euler explicit time differencing,

$$y^{n+1} = y^n + \Delta t\, y^n(1 - y^n) = f(y^n). \tag{4}$$

Prüfer [17] points out that Eq. (4) may be transformed into Eq. (1) by substituting $z^n = (\Delta t/(1 + \Delta t))\, y^n$ and $R = 1 + \Delta t$. Since we know Eq. (1) has the behavior shown in Fig. 10, then for some Δt the solution given by Eq. (4) will behave chaotically for some initial conditions. The true solution, given by Eq. (3), is well behaved, as is clear from Fig. A1.

Let us examine the linear stability of the discrete approximation given by Eq. (4). Linearizing Eq. (4) about the fixed point $y = 1$ yields

$$\tilde{y}^{n+1} = (1 - \Delta t)\, \tilde{y}^n \tag{5}$$

which has the linear stability bound $\Delta t \leqslant 2$. The location of

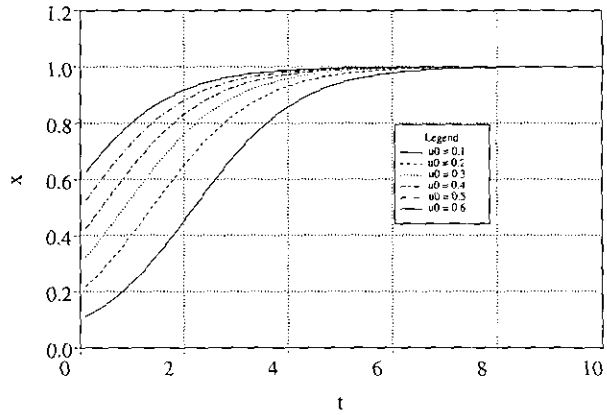

FIG. A1. Solutions from different initial conditions for Eq. 2.

the bifurcation to the first period-two solution for the iterative map is determined by solving the nonlinear system

$$u = f(v), \qquad v = f(u)$$

for u, v in terms of Δt. The critical point y_c is given by

$$y_c = \frac{(2 + \Delta t) \pm \sqrt{(\Delta t)^2 - 4}}{2\Delta t},$$

which only has real solutions for $\Delta t > 2.0$, coinciding with the linear stability bound. In this case the linear instability bound is also the point at which the discrete map approximation of the ODE bifurcates to a period-two solution. Other discrete approximations to the Eq. (3) also have linear stability bounds coinciding with bifurcation boundaries, although this may not always be the case. For example, MacCormack's scheme has the linear stability bound $\Delta t \leqslant 2.0$ and bifurcation boundary $\Delta t > 2.0$, but it has a different bifurcation map past the boundary than

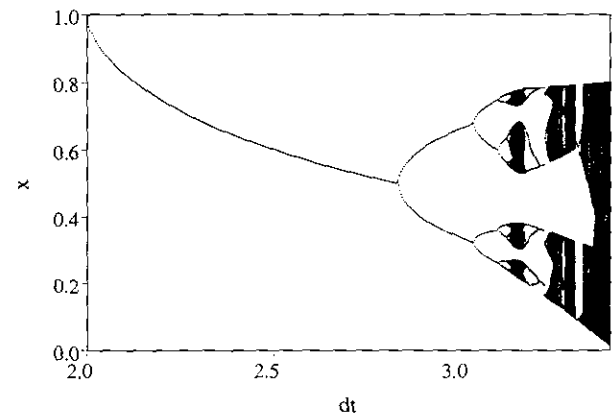

FIG. A2. Quadratic like chaotic map for MacCormack's scheme.

Euler explicit (i.e., the logistic map), see Fig. A2 for the lower half of the bifurcation diagram past $\Delta t = 2$.

Stuart [19] has studied systems of nonlinear PDEs and has shown that for a fairly general class of nonlinear reaction–diffusion equations, linearized instability leads to spurious periodic solutions in the nonlinear discretization.

These results are rather interesting in that they imply that there is a region of time steps where the solution is bounded but not convergent to the correct solution. Above a certain time step, one obtains the expected response of unbounded growth, but between the linear stability bound and the unstable limit the numerical solution can behave as above, i.e., chaotically. This implies that in some situations, a new region of "unusual" stability can be defined. An example where one may take advantage of this behavior would be for stiff reaction equations where one part of a system lies in this bounded (but chaotic) region and other parts in the fixed-point region. This opens up a new avenue of research into "nonlinear stability theory" which extends the usual "linear stability bounds." In practice, numerical analysts rely upon linear stability theory to determine limits for integrations. But this new area, especially when applied to basicly nonlinear equations such as the Navier–Stokes equations, may lead to new understanding and algorithms.

REFERENCES

1. D. Ruelle and F. Takens, *Commun. Math. Phys.* **20**, 167 (1971).
2. E. Lorenz, *Physica D* **35**, 299 (1989).
3. C. Sparrow, *The Lorenz Equations: Bifurcations, Chaos, and Strange Attractors*, Applied Mathematical Sciences, Vol. 41, (Springer-Verlag, New York, 1982).
4. A. Brandstater, J. Swift, H. L. Swinney, A. Wolf, J. D. Farmer, E. Jen, and J. P. Crutchfield, *Phys. Rev. Lett.* **51**, 1442, (1983).
5. J. A. Vastano and R. D. Moser, *J. Fluid Mech.* **233**, 83 (1991).
6. L. Keefe, P. Moin, and J. Kim, *American Physical Society Bull.* **32**, 2026 (1987).
7. K. Stuber, Ph.D. thesis, University of California at San Diego, La Jolla, 1988 (unpublished).
8. A. Fortin, M. Fortin, and J. J. Gervais, *J. Comput. Phys.* **70**, 295 (1987).
9. K. N. Ghia, G. A. Osswald, and U. Ghia, "Simulation of Self-Induced Unsteady Motion in the Near Wake of a Joukowski Airfoil", in *Lecture Notes In Engineering, Vol. 24*, edited by K. Kuwahara, R. Mendz, and S. A. Orzag (Springer-Verlag, New York/Berlin, 1986), p. 118.
10. T. H. Pulliam, "Efficient Solution Methods for the Navier–Stokes Equations," in *Lecture Notes for the von Kármán Institute for Fluid Dynamics Lecture Series: Numerical Techniques for Viscous Flow Computation in Turbomachinery Bladings, von Kármán Institute, Rhode-St-Genese, Belgium, 1985* (unpublished).
11. T. H. Pulliam, *AIAA J.* **24**, 1931 (1986).
12. F. Takens, in *Dynamical Systems of Turbulence*, Lecture Notes in Mathematics, Vol. 898, edited by D. A. Rand and L. S. Young (Springer-Verlag, New York/Berlin, 1981), p. 366.
13. M. J. Feigenbaum, *J. Statist. Phys.* **19**, 25 (1978).
14. P. Frederickson, J. L. Kaplan, E. D. Yorke, and J. A. Yorke, *J. Differential Equations* **49**, 185 (1983).
15. P. Grassberger and I. Procaccia, *Physica D* **9**, 89 (1983).
16. A. Wolf, J. B. Swift, H. L. Swinney, and J. A. Vastano, *Physica D* **16**, 285 (1985).
17. M. Prüfer, *SIAM J. Appl. Math.* **45**, 32 (1985).
18. E. Lorenz, *Physica D* **35**, 299 (1989).
19. A. Stuart, *IMA J. Numer. Anal.* **9**, 465 (1989).